Simulating the Mott transition on a noisy digital quantum computer via Cartan-based fast-forwarding circuits

Thomas Steckmann,[1] Trevor Keen,[2] Alexander F. Kemper,[1] Eugene F. Dumitrescu,[3] and Yan Wang[3]

[1]*Department of Physics, North Carolina State University, Raleigh, North Carolina 27695, USA*
[2]*Department of Physics and Astronomy, University of Tennessee, Knoxville, TN 37996*
[3]*Quantum Computational Science Group, Oak Ridge National Laboratory, Oak Ridge, Tennessee 37831, USA*
(Dated: December 5, 2021)

Dynamical mean-field theory (DMFT) maps the local Green's function of the Hubbard model to that of the Anderson impurity model and thus allows solving the Hubbard model by solving the simpler quantum impurity model. Quantum algorithms have been proposed to efficiently solve impurity models by preparing and evolving the ground state under the impurity Hamiltonian, which is the most expensive part of the calculation for DMFT. We propose a highly optimized fast-forwarding quantum circuit to significantly improve quantum algorithms for the minimal DMFT problem. Our Cartan decomposition-based algorithm uses a fixed depth quantum circuit to eliminate time-discretization errors and evolve an initial state over *arbitrary* time. Exploiting the structure of the fast-forwarding circuits, we sufficiently reduce the gate cost to simulate the dynamics of, and extract frequencies from, the Anderson impurity model on noisy quantum hardware and demonstrate the Mott transition by mapping the phase-diagram of the impurity problem. Especially near the Mott phase transition when the quasiparticle resonance frequency approaches zero and evolving the system over long-time scales is necessary, our method maintains accuracy where Trotter error would otherwise dominate. By accurately computing the DMFT phase diagram on a digital quantum computer we open up the way for more sophisticated techniques to solve more complex correlated electronic phenomena.

I. INTRODUCTION

Using quantum computers to accurately model the behavior of strongly correlated quantum systems is one of the most promising near-term applications of noisy intermediate scale quantum (NISQ) computers. In contrast, Shor's algorithm [1] for factoring large numbers will require thousands of nearly-noiseless qubits to become practically useful. On the other hand, quantum simulations of fermions only require $\sim$100 qubits to potentially surpass classical simulation methods. Proposals for simulating correlated fermionic systems using quantum computers exist check Bassman QST review [2–6] but relatively few have been implemented or tested due to the noise of current devices [7–9].

Within condensed-matter physics a wide variety of correlated systems can be mapped to correlated *impurity* models by embedding methods such as dynamical mean field theory (DMFT). Even though the DMFT impurity mapping simplifies many problems, classical simulations based on exact diagonalization are still limited to dozens of orbitals [10] due to the exponential growth of correlations and the corresponding Hilbert space which requires an exponential amount of memory to store the quantum many-body state. Other methods, such as quantum Monte Carlo (QMC) [11] and matrix product state (MPS) [12] methods, also suffer from some sort of exponential complexity scaling making them intractable. In the case of QMC, the fermion sign problem [13] has been shown to be NP-hard in general and limits simulations to high temperatures. Matrix product state methods, on the other hand, suffer from entanglement issues for certain geometries [12]. Quantum computers alleviate this exponential scaling by instead storing many-body quantum states with memory resources scaling polynomially with the system size.

Prior work studying the dynamics of interacting electrons via DMFT observed that even over very small time scales Trotter approximate time evolutions lead to nonphysical results: comparing to theoretical values, simulations on the quantum computer give inaccurate frequencies of the time evolution for the two-site DMFT, which are symptoms of decoherence or approximation errors [9]. For NISQ systems, the Trotter approximation leads to a dilemma: theoretically it becomes exact in the limit of an infinite-depth circuit, so more accurate simulations require increased gate counts, but increasing gate count reduces simulation fidelity due to accumulated noise. The hardware requirements needed to achieve reliable updates in the DMFT loop using the Trotter decomposition of the time-evolution operator has been analyzed in Ref. 14. In Ref. 8, the authors use a variational quantum eigensolver (VQE) to implement an

exact diagonalization solver for the two-site DMFT problem. This method works well for two-site DMFT after a regularization technique is used to remove the unphysical pole that arises from small errors.

In this work, we approach the problem of solving the two-site DMFT problem by utilizing a Lie-algebraic method to fast-forward the the dynamics of the Anderson Impurity Model (AIM). Our method, based on a Cartan decomposition of the algebraic closure of the Hamiltonian, compiles the time evolution operator into a fixed depth circuit for any chosen simulation time; therefore, the error from the quantum device is independent of the length of the time evolution of the system and a one-time decomposition performed on a classical computer allows for arbitrarily low numerical error in the parameters of the decomposed factors. As described in Ref. 15, given a Hamiltonian $\hat{H}$, the Cartan decomposition requires finding a particular sequence of unitary rotations which, when contracted, span and parameterize the time-evolution unitary $e^{-it\hat{H}}$ of a target system for all time t. The Cartan decompostion generalizes the polar and singular-value decompositions at the level of groups and provides a mapping from the required dynamics onto two sets of parameterized unitaries.

We first review and motivate the quantum impurity model and provide a hybrid quantum-classical algorithm solving it. We then apply group analysis to fast-forward the dynamical simulation on a quantum computer. The structure of Cartan decomposition allows for further simplifications which result in a highly optimized circuit that can be tailored to execute on specific hardware architectures. We then perform simulations at vastly different time scales which allow us to accurately extract both low and high frequency Green's functions for the two-site DMFT on NISQ hardware. This enables us to demonstrate for the first time a Mott-insulating phase transition in the Hubbard model via a digital quantum simulation on quantum hardware.

II. MODEL HAMILTONIANS

A. Hubbard model

The Fermi-Hubbard model has no known exact solution in more than one dimension, even though it is one of the simplest to express models that capture interactions between electrons. Despite its relative simplicity, the Hubbard model accounts for many interesting phenomena in condensed matter physics, including the Mott metal-insulator transition [16–18], antiferromagnetism [19], emergent spin and stripe orders [20, 21], strange metallic behavior [22], pseudogaps [23, 24], and high-temperature superconductivity [23, 25].

The single-band Fermi-Hubbard model Hamiltonian is given by

$$\hat{H} = -\tilde{t} \sum_{\langle i,j \rangle, \sigma} (\hat{c}_{i\sigma}^\dagger \hat{c}_{j\sigma} + \hat{c}_{j\sigma}^\dagger \hat{c}_{i\sigma}) + U \sum_i \hat{n}_{i\uparrow} \hat{n}_{i\downarrow} - \mu \sum_{i,\sigma} \hat{n}_{i,\sigma}, \tag{1}$$

where $\hat{c}_{i\sigma}^\dagger$ ($\hat{c}_{i\sigma}$) is the electron creation (annihilation) operator for electron with spin $\sigma \in \{\uparrow, \downarrow\}$ at lattice site i; $\hat{n}_{i\sigma} = \hat{c}_{i\sigma}^\dagger \hat{c}_{i\sigma}$ is the electron density operator; $\tilde{t}$ is the hopping integral ("tunneling") which we typically choose as the unit of energy by setting $\tilde{t} = 1$; U models the Coulomb interaction with an on-site double occupancy interaction cost; and μ is the chemical potential. Here, $\langle i,j \rangle$ refers to indices of nearest-neighbor sites on the lattice [26]. The Hubbard model has been recently investigated in the context of quantum computing with applications to VQE algorithms [27, 28] and as a benchmark for for quantum simulations [4, 29, 30].

B. Anderson impurity model and dynamical mean-field theory

Exact simulations of the Hubbard model in the general case are limited to dozens or hundreds[AFK: Are particles electrons here? and is there a citation for hundreds?] of particles [31, [YW: or any other state-of-the-art work to be cited here?]], far from the large number of particles which would be considered in the macroscopic (thermodynamic) limit. Dynamical mean-field theory is a significant development in studying the Hubbard model for larger systems [32]. In the limit of a lattice with infinite dimensions (∞-d), such as ∞-d hypercubic Bethe lattice with infinite coordination number, DMFT exactly maps the solution of the Hubbard model to that of the Anderson impurity model, where the temporal correlations are accurately captured. The interacting electrons in the Hubbard model in the thermodynamic limit (i.e., *infinite* lattice sites) are reduced to electrons interacting on a single impurity site coupled to an electronic bath of *continuous* levels that tunnel into the impurity site. We describe the energy levels using N_b discrete bath lattice sites with on-site energy ϵ_i and index $i \in \{1, \ldots, N_b\}$. Since we will consider nonmagnetic states, these parameters

do not depend on the electron spin quantum number. The Anderson impurity model Hamiltonian is then given by

$$\hat{H}_{\text{AIM}} = \sum_{i=1,\sigma}^{N_b} V_i(\hat{c}_{0,\sigma}^\dagger \hat{c}_{i,\sigma} + \hat{c}_{i,\sigma}^\dagger \hat{c}_{0,\sigma}) + U\hat{n}_{0,\uparrow}\hat{n}_{0,\downarrow} + \sum_{i=0,\sigma}^{N_b} (\epsilon_i - \mu)\hat{n}_{i,\sigma}, \tag{2}$$

where V_i is the coupling (tunneling) between the impurity site (site index 0) and bath sites. The Coulomb interaction (U) term only involves the impurity site. The minimal non-trivial approximation of the Hubbard model dynamics is two-site DMFT, which includes a single bath site ($N_b = 1$) and a single impurity site. This is the problem we will consider.

Using X_i, Y_i, Z_i to denote the Pauli operator acting on site i, a Jordan-Wigner spin-fermion transformation (Appendix A) maps the AIM Hamiltonian in fermion operators to the spin Hamiltonian in Pauli operators as follows.

$$\hat{H}_{\text{AIM}} = \frac{V}{2}(X_0 X_1 + Y_0 Y_1 + X_2 X_3 + Y_2 Y_3) + \frac{U}{4}Z_0 Z_2, \tag{3}$$

which has been simplified for the case of particle-hole symmetry and a half-filled ground state by setting $\mu = \frac{U}{2}$, $\epsilon_0 = 0$, and $\epsilon_1 = \frac{U}{2}$.

III. ALGORITHM AND METHODS

A. Algorithm for computing Green's function

In DMFT, the dynamics and response of the interacting electron system is described by the *retarded impurity Green's function* which is denoted as $G_{\text{imp}}^R(t)$ in the time domain

$$G_{\text{imp}}^{\text{R}}(t,t') = -i\theta(t-t') \langle \psi_0 | \{\hat{c}_{0,\sigma}(t), \hat{c}_{0,\sigma}^\dagger(t')\} | \psi_0 \rangle. \tag{4}$$

In the Heisenberg picture, operators $\hat{c}(t)$ are time evolved as $\hat{c}(t) = U^\dagger(t)\hat{c}U(t) = e^{it\hat{H}}\hat{c}e^{-it\hat{H}}$. Due to time translation invariance, we simplify the computation by setting $t' = 0$. This Green's function describes the propagation of a perturbation of the system as the system evolves. We consider injecting (removing) a particle into (from) the impurity site with respect to the ground state of the system at zero temperature and removing (injecting) a particle at the impurity site some time later and computing the overlap with the initial state. There are two possibilities of injecting or removing a spin-↑ particle or a spin-↓ particle, corresponding to the spin-↑ and spin-↓ impurity Green's functions, respectively. The half-filled ground state has zero total spin and is spin-rotationally invariant, so spin-↑ and spin-↓ Green's functions behave identically. We therefore focus the spin-↑ impurity Green's function below.

In Appendix B we elaborate on the full expansion and subsequent simplification of Green's function after the Jordan-Wigner transform is applied, which results in the relatively inexpensive expectation

$$iG_{\text{imp}}^{\text{R}}(t > 0) = \text{Re}\left[\langle \psi_0 | U^\dagger(t) X_0 U(t) X_0 | \psi_0 \rangle\right]. \tag{5}$$

This term can be evaluated with the expectation of a single Hadamard-test type quantum circuit using only one time evolution operator in the circuit.

1. Iteration loop for DMFT

The DMFT mapping is a self-consistent mapping, requiring multiple iterations where the DMFT parameters V_i and ϵ_i are updated from an initial guess of the Anderson impurity model until the system reaches self-consistency. For each new iteration, the V_i and ϵ_i computed in the previous iteration are put into the impurity model, which is then solved and the solution used to recompute the DMFT parameters. The iteration loop continues until the recomputed values are sufficiently close to the previous values of V_i and ϵ_i. For the two-site model, particle-hole symmetry and knowledge of the general form for the solution provide a mechanism for reducing the cost of the computation and the accuracy of convergence. The form of the DMFT loop used for our calculations can be summarized as follows and is represented in figure 1:

1. Choose initial values for parameters V_i and ϵ_i. Due to half-filling of the two-site model, the values for ϵ_0 and ϵ_1 are fixed and do not need to be updated.
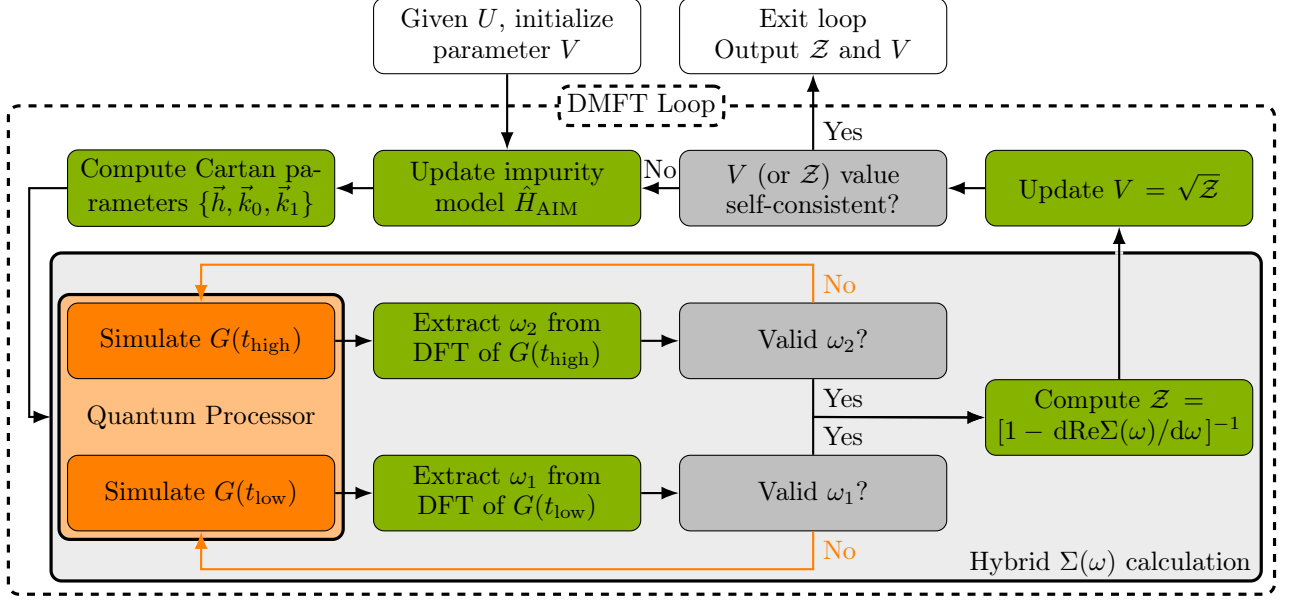
FIG. 1: Diagram of the DMFT loop, as implemented in the two-site calculation. Our procedure was initialized with $V = 0.5$, and for each DMFT loop iteration recomputes the parameters for the Cartan decomposition for the new value of V. The hybrid computation of $\Sigma(\omega)$ evaluates the two frequencies ω_1 and ω_2 separately, in a procedure that is elaborated on in section IV(C).

2. On the quantum computer, evaluate the retarded impurity Green's function $G_{\mathrm{imp}}^R(t)$ for a selection of time t values. In the two-site model, the evaluated function will have the form

$$-iG_{\mathrm{imp}}^R(t > 0) = 2[\alpha_1 \cos(\omega_1 t) + \alpha_2 \cos(\omega_2 t)] \tag{6}$$

where ω_1 is the quasi-particle resonance frequency and ω_2 is the Hubbard band [33].

3. Compute the discrete Fourier transform (DFT) of Green's function, giving $G_{\mathrm{imp}}^R(\omega)$.

4. Compute the self-energy $\Sigma_{\mathrm{imp}}(\omega)$ using $G_{\mathrm{imp}}^R(\omega)$. We have the general result [34]

$$G_{\mathrm{imp}}^R(\omega) = \frac{1}{\omega + i\delta - (\epsilon_0 - \mu) - \Delta(\omega) - \Sigma_{\mathrm{imp}}(\omega)}. \tag{7}$$

which introduces an artificial broadening term $i\delta$. $\Delta(\omega)$ is the mean-field-like hybridization function

$$\hat{\Delta}(\omega) = \frac{V^2}{\omega - (\epsilon_1 - \mu) + i\delta}. \tag{8}$$

Dyson's equation $G_{\mathrm{imp}}^R(\omega) = G_{\mathrm{imp}}^{R(0)}(\omega) + G_{\mathrm{imp}}^{R(0)}(\omega)\Sigma_{\mathrm{imp}}(\omega)G_{\mathrm{imp}}^R(\omega)$, along with the result in Eq. (7) provides an analytic solution

$$\Sigma_{\mathrm{imp}}(\omega) = \frac{1}{G_{\mathrm{imp}}^{R(0)}(\omega)} - \frac{1}{G_{\mathrm{imp}}^R(\omega)}, \tag{9}$$

Here, $G_{\mathrm{imp}}^{(0)}(\omega)$ is the non-interacting Green's function with $U = 0$. In the frequency domain, this is exactly

$$G_{\mathrm{imp}}^{R(0)}(\omega) = \frac{1}{\omega - \left(\epsilon_0^{(0)} - \mu^{(0)}\right) - \Delta(\omega)} = \frac{1}{\omega - \Delta(\omega)}. \tag{10}$$

5. From the self-energy, compute the quasi-particle weight $\mathcal{Z}$ and update $V_{\mathrm{new}} = \sqrt{\mathcal{Z}}$. In this work, we use the

value of the quasi-particle weight computed using the derivative of the self-energy at zero frequency:

$$\mathcal{Z}^{-1} = 1 - \left.\frac{\mathrm{dRe}[\Sigma_{\mathrm{imp}}(\omega)]}{\mathrm{d}\omega}\right|_{\omega=0} \tag{11}$$

Prior work on this topic by Keen *et al.* [9] computed the quasi-particle weight as the integral of the spectral function $A(\omega) = -\frac{1}{\pi}Im[G_{\mathrm{imp}}^R(\omega)]$ over the low frequency peaks

$$\mathcal{Z} = \int_{|\omega \pm \omega_1| < 4\delta} A(\omega)\, \mathrm{d}\omega\,, \tag{12}$$

in order to mitigate noise sources. We initially observed a numerical instability in computing $\mathcal{Z}$ using Eq. (11) which arises from taking the derivative of the self-energy computed using $G_{\mathrm{imp}}^R(t)$ fitted to Eq. (6) without analytically exact solutions for the parameters. Instead of computing the derivative in Eq. (11) numerically, we solve the derivative analytically in Appendix C by using the exact Fourier integral transform of Eq. (6), remove the unphysical simple pole of self-energy by assuming a condition obeyed by the exact solution $\frac{2\alpha_1}{\omega_1^2} + \frac{2\alpha_2}{\omega_2^2} = \frac{1}{V^2}$, and finally find Eq. (13), which is equivalent to Eq. (14) that depends only on the parameters ω_1 and ω_2. In converting Eq. (13) to Eq. (14), we use the spectral function sum rule $2\alpha_1 + 2\alpha_2 = 1$.

$$\mathcal{Z} = \frac{2(\alpha_1\omega_2^2 + \alpha_2\omega_1^2)^2}{\alpha_1\omega_2^4 + \alpha_2\omega_1^4} \tag{13}$$

$$= \frac{\omega_1^2\omega_2^2}{V^2(\omega_1^2 + \omega_2^2 - V^2)}. \tag{14}$$

2. Cartan decomposition

Our primary contribution is simplifying the time evolution unitary operation $\exp\left(-it\hat{H}_{\mathrm{AIM}}\right)$ in the Green's function measurement circuit by applying Cartan decomposition. The standard method based on Trotterization is an approximation of the time evolution circuit which converges in the limit of an infinite depth circuit. Though there are different methods of approaching a Trotter time evolution, the first order approximation is typically applied [9, 14, 34]:

$$e^{-it\hat{H}} = \left(e^{-i\frac{t}{N}\hat{H}}\right)^N \approx \left(\prod_{l=1}^M e^{-i\frac{t\beta_l}{N}b_l}\right)^N \tag{15}$$

where $\hat{H} = \sum_{l=1}^M \beta_l b_l$ with $\beta_l \in \mathbb{R}$ and b_l is a Pauli string.

The fast-forwarding algorithm used in our time-evolution operator is based on the application of an algorithm for performing Cartan decomposition. Here, we briefly summarize the algorithm applied to $\hat{H}_{\mathrm{AIM}}$ given in Eq. (3) and also illustrate the steps in Fig. 2. We denote a (real) Lie algebra and its elements by lowercase Gothic (Fraktur) and Roman characters, respectively, such as $\mathfrak{g}$ and $ig \in \mathfrak{g}$, where g is a simple n-qubit Pauli string or a linear combination of them (with real coefficients). Here, we use the physicists' convention with a pre-factor i in the Lie algebra elements. SU(2^n) group elements are denoted by uppercase Roman characters, e.g., $G = \exp(ig)$. The goal is to find a factorization of the unitary operator by use of the KHK theorem, which states that the unitary may be written as

$$e^{-it\hat{H}} = e^{ik}e^{-ith}e^{-ik} \tag{16}$$

where k and h are elements of a Cartan decomposition (see below). Note that the time argument t only appears in one factor. The general steps to obtain the Cartan form of the time-evolution operator are detailed in Refs. 15 and 35; we briefly summarize them here for completeness.

1. Generate the *Hamiltonian algebra* $\mathfrak{g}(\hat{H})$. This is a Lie algebra over the field $\mathbb{R}$ that is generated by the closure of commutators (Lie brackets) of ib_l, where b_l's are individual n-qubit Pauli string terms of the Hamiltonian $\hat{H} = \sum_l \beta_l b_l$, ($\beta_l \in \mathbb{R}$). $\mathfrak{g}(\hat{\mathfrak{H}}$ a subalgebra of $\mathfrak{su}(2^n)$.

2. Find a Cartan decomposition $\mathfrak{g} = \mathfrak{k} \oplus \mathfrak{m}$ of the Hamiltonian algebra $\mathfrak{g}(\hat{H})$ such that $i\hat{H}$ lies in $\mathfrak{m}$. Here, $\mathfrak{k}$ is a subalgebra of $\mathfrak{g}(\hat{H})$.
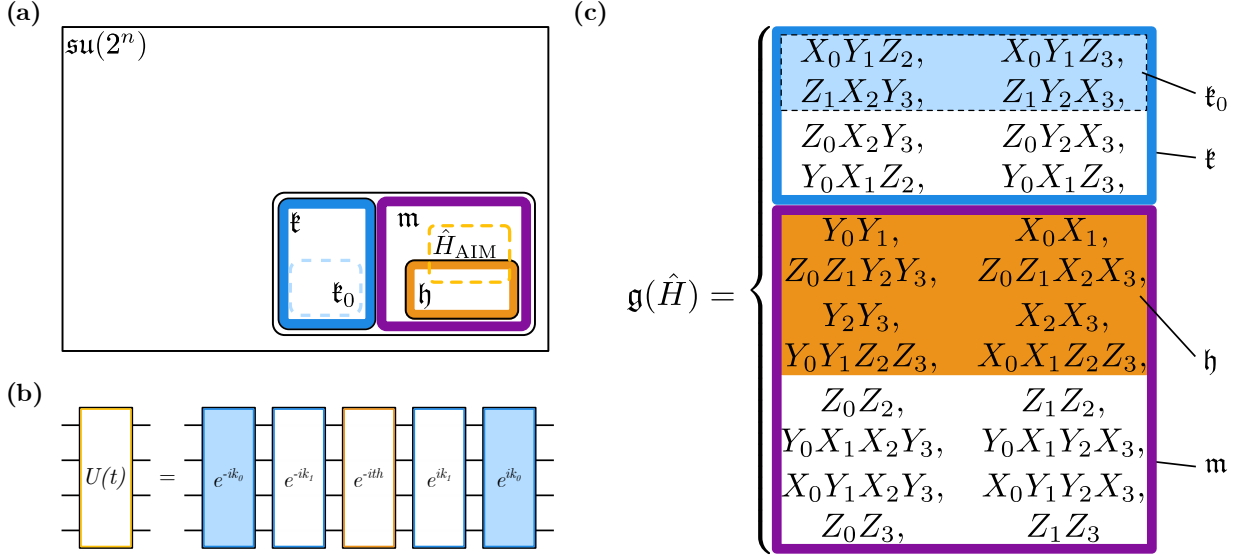
FIG. 2: (a) A generalized diagram of the Cartan decomposition of the Hamiltonian algebra with dimension $= 24$ within the special unitary algebra with dimension $= 255$. Here, $\mathfrak{k}_o$ is the set of basis elements which commute with X_0, which is not a typical requirement of Cartan decomposition but results in a significant gate cost reduction in our application. (b) A block circuit diagram of the decomposed time evolution operator. (c) Cartan decomposition applied to the AIM Hamiltonian Eq. (A1), where the blue, shaded light blue, magenta, and shaded orange color regions correspond to the sets $\mathfrak{k}, \mathfrak{k}_o, \mathfrak{m}$, and $\mathfrak{h}$.

3. From $\mathfrak{m}$ find a maximal Abelian subalgebra $\mathfrak{h}$, which is called a *Cartan subalgebra* of the pair $(\mathfrak{g}, \mathfrak{k})$.

4. Find a local extremum over the algebra $\mathfrak{k}$ of $f(k) = \langle e^{ik}(v)e^{-ik}, \hat{H} \rangle$. Here, $\langle a, b \rangle$ is the Killing form which is proportional to $\text{Tr}(ab)$ for $a, b \in \mathfrak{su}(2^n)$. ik is an element of $\mathfrak{k}$ written as a sum of Pauli strings $k = \sum_j \chi_j \kappa_j$ where $i\kappa_i$ form a basis for $\mathfrak{k}$. The optimization is performed over the coefficients χ_j. v is a fixed element in $\mathfrak{h}$: $v = \sum_j \gamma^j h_j$ where ih_j are Pauli strings that form a basis for $\mathfrak{h}$, and γ is a transcendental number such as π. Here, γ^j is the $j-$th power of γ.

5. Compute the vector $e^{-ik}(i\hat{H})e^{ik} = ih$.

The results of the algorithm are the elements $ih \in \mathfrak{h}$ and $ik \in \mathfrak{k}$ which satisfy $e^{-it\hat{H}} = e^{ik}e^{-ith}e^{-ik}$. Often, additional decomposition is required to implement e^{ik} using a universal gate set, but in the case of two-site DMFT $\mathfrak{k}$ is Abelian. Because h is always composed of commuting elements, the full exponential is relatively simple to implement exactly on a quantum computer. We note that the dimensionality of the Hamiltonian algebra generated by the $\hat{H}_{\text{AIM}}$ scales exponentially with the number of bath sites. However, for the two-site model, the size of the algebra remains manageable. It is of continuing interest to determine if the dimensionality of the Hamiltonian algebra can be constrained to polynomial in the number of bath sites by adopting some effective approximate algorithm.

Analysis of the terms in $\mathfrak{k}$ resulting from the Cartan decomposition in figure 2(c) reveals that we can divide $\mathfrak{k}$ into a set of basis elements which commute with X_0, which we call $\mathfrak{k}_0$, and the elements which do not, which we call $\mathfrak{k}_1$. This construction later leads to a reduction in the circuit construction, but we highlight the partition here as an operation which is only possible due to the specific form of the Cartan decomposed time evolution operator.

IV. HARDWARE IMPLEMENTATION

The general circuit used to evaluate Green's function is constructed using three major components. First, the system qubits must be instantiated in the ground state $|\psi_0\rangle$. The Green's function expectation is then evaluated using measurements on an ancilla qubit introduced through a Hardamard-test-like interference circuit [34, 36]. The interference circuit used allows for the operator $X_0(t)$ to be implemented using only a single instance of a time-evolution operator, which is itself implemented using the sequence Pauli exponential gates determined using a set of Cartan decomposition solutions k_0, k_1, and h. These parameters are updated once per iteration of the DMFT loop when the Hamiltonian is updated.
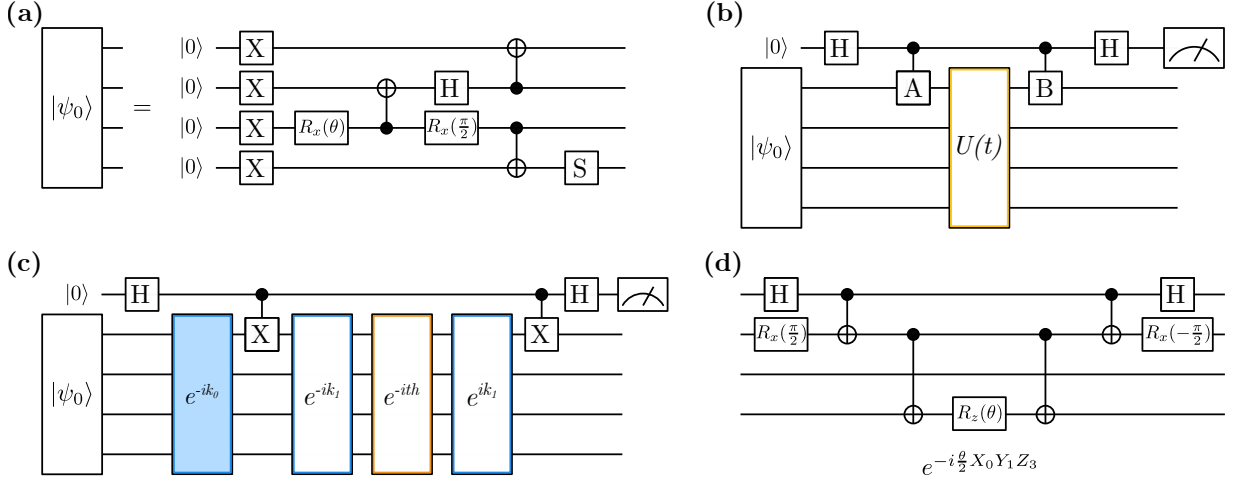
FIG. 3: (a) Ansatz circuit used to prepare the ground state. (b) General Hadamard interference type circuit used to compute $\text{Re}[\langle B(t)A\rangle]$. (c) Block decomposed Green's function circuit used in the final computation, except for the ordering and coefficients of the $\mathfrak{k}$ and $\mathfrak{h}$ exponentials. The property of k_0 allows for commuting through the CNOT gate so it need only be implemented once. (d) A general circuit showing the implementation of a Pauli gate exponential.

A. Circuit components

Our ground state for all values of V and U was initialized using the ansatz circuit in figure 3(a), constructed from only a single variational parameter and 3 nearest neighbor CNOTs. It is the simplest known circuit to prepare the required states. The value θ is determined by minimizing the energy through a simulated Variational Quantum Eigensolver. A generic circuit used for evaluating terms of the form $\langle \hat{B}(t)\hat{A}\rangle$, like that in $Eq.$ (5), is included in figure 3(b) [9, 34, 36]. The real component of the expectation is determined through a measurement on the ancilla qubit: $\text{Pr}(0_a) - \text{Pr}(1_a) = \langle Z_a\rangle$. The corresponding imaginary component, which is not required for our purposes, is evaluated as $\langle Y_a\rangle$ and uses an additional $R_x(\pi/2)$ gate after the final Hadamard gate in figure 3(b). The Cartan decomposition is computed using the Cartan Quantum Synthesizer Python package [37]. For a given solution $k = \sum_j \chi_j k_j$ to the cost function $f(k)$ for the Cartan decomposition and the corresponding element $h = \sum_j \eta_j h_j$, the time evolution operator is implemented using a sequence of single Pauli string exponential of the form in figure 3(d): for example, $e^{it(\sum_j \eta_j h_j)} = \prod_j e^{it\eta_j h_j}$. The additional decomposition $k = k_0 + k_1$ is applied to the element k, and the circuit implemented in figure 3(c) follows from commuting e^{ik_0} through X_0 as follows.

$$\langle U(-t)X_0U(t)X_0\rangle = \langle\psi_0|\left(e^{ik_0}e^{ik_1}e^{ith}e^{-ik_1}e^{-ik_0}\right)X_0\left(e^{ik_0}e^{ik_1}e^{-ith}e^{-ik_1}e^{-ik_0}\right)X_0|\psi_0\rangle$$
$$= \langle\psi_0 e^{ik_0}|\left(e^{ik_1}e^{-ith}e^{-ik_1}\right)X_0\left(e^{-ik_0}e^{ik_0}\right)\left(e^{ik_1}e^{-ith}e^{-ik_1}\right)X_0|e^{-ik_0}\psi_0\rangle \tag{17}$$

Thus instead of preparing as the inital state $|\psi_0\rangle$, we prepare $e^{-ik_0}|\psi_0\rangle$ and time evolve using $e^{ik_1}e^{-ith}e^{-ik_1}$. A combination of manual and algorithmic transpiling through Qiskit reduces the full cost of the final circuit to 77 nearest neighbor CNOTs [38].

B. Error mitigation

Beyond the noise reductions gained through careful compiling of the circuit, we implement three methods in an effort to mitigate errors during the run-time. First, randomized Cartan solutions are employed in an effort to mitigate coherent noise, especially the noise due to over rotation of the entangling gates [39]. The minimization of $f(k)$ over different initial conditions yields distinct solutions for k at the minimum. We observe that averaging the Green's function measurements from two or more values of k at each time serves to reduce the error in the evaluation. In this work, we use two different solutions to the Cartan decomposition.

The second method to reduce error, measurement error mitigation, serves as an initial step in correcting noise in the experiment results and we process the quantum measurements through the native procedure in Qiskit [38, 40].

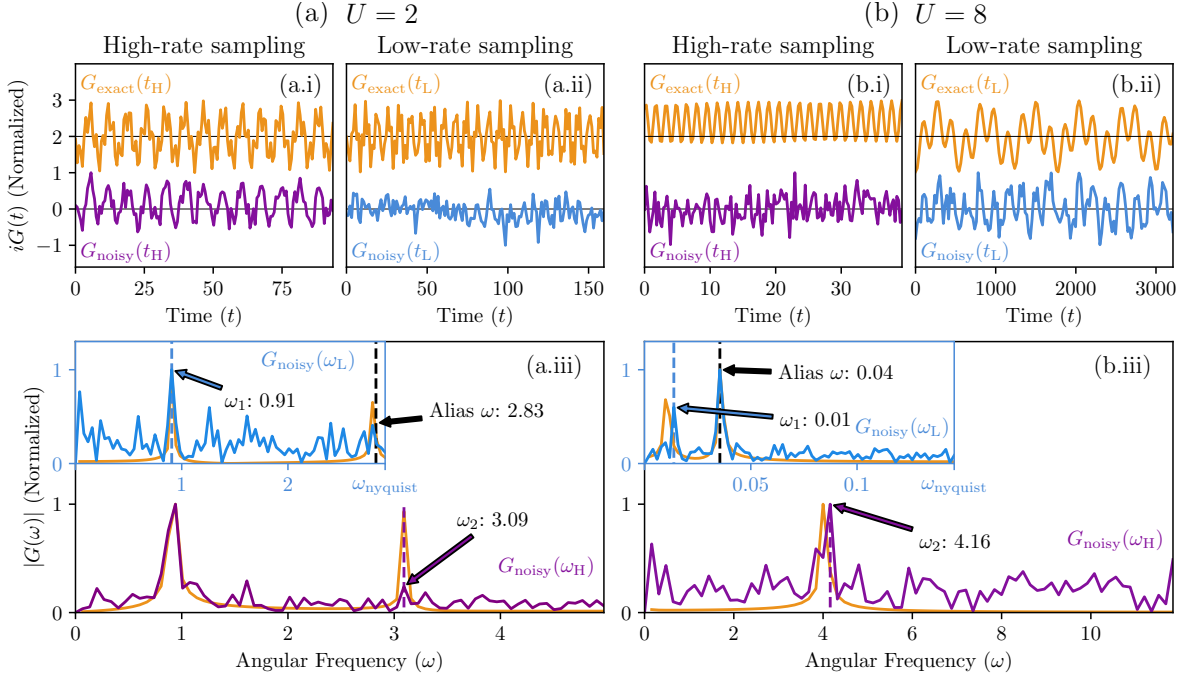The final, and most significant error mitigation technique, follows from measurements on the system, or wavefunc-

FIG. 4: Green's function sampled on the quantum computer *ibmq_ manila* at self-consistency. Initial Conditions: (a) $U = 2$ and $V_{\text{initial}} = 0.964$ and (b) $U = 8$ and $V_{\text{initial}} = 0.119$. (i/ii) The normalized Green's function with a phase correction (top, shifted vertically) and the actual, noisy results (bottom) sampled with high (t_H) and low (t_L) frequencies to evaluate the high frequency signal ω_2 and and the low frequency signal ω_1, respectively. (iii) The discrete Fourier transform showing the ideal frequencies (solid, orange) and the evaluated peaks (dashed) for both frequencies. Spurious peaks at $\omega = 0$ have been removed. (a) Returns a value of $V_{\text{new}} = 0.944$ and (b) returns a value of $V_{\text{new}} = 0.116$, both within the tolerance of 0.02.

tion, qubits. The Hadamard-test type circuit does not use or require a measurement of these qubits, instead assuming that the wavefunction qubits are traced out of the final circuit before measuring $\langle Z_a \rangle$. The partial trace operation is equivalent to simply measuring the resulting wavefunction state in the Z basis. Indeed, the final state of the wavefunction qubits is a superposition of $|\psi_0\rangle$ and $X_0(t)X_0 |\psi_0\rangle$, both of which we expect to have the same particle number and total spin as the original state $|\psi_0\rangle$. The initial state is known to have two fermions with a total spin zero, so for each shot in the evaluation of Green's function, we evaluate if the final measurement of the wavefunction state maintains both parameters, discarding the shot if either condition is violated. This corresponds to checking for an odd number of bit-flip errors in the wavefunction qubits which we expect to affect the final ancilla measurement. On the quantum hardware used in this work, *ibmq_ manila*, approximately 65% of the circuit evaluations are discarded due to this correction, which is applied after all other error mitigation techniques.

C. DMFT loop

Evaluation of Green's function and the convergence of the DMFT loop requires minimizing errors and evaluating a series of discrete time points sufficient to determine both the low frequency signal ω_1 and the high frequency signal ω_2. Generally, these two criteria are contradictory to a third consideration of the run-time for the evaluation. That is, increasing the number of shots, the number of randomized Cartan solutions, and the discrete time points evaluated corresponds to increasing accuracy in convergence but significantly increased run-time. Above the critical $U_c = 6$, the frequency ω_1 and the corresponding amplitude α_1 converge to 0 at self-consistency. Consequently, for any set of discrete time steps t_H with a nyquist rate above the high frequency $\omega_2 = \frac{U}{2}$ at self-consistency, sampling to a sufficiently long time to distinguish the low frequency signal ω_1 is prohibitively expensive. For example, finding $\omega_1 = .01 \pm .005$ with $U = 8$ requires over 5,000 evaluations using a sampling rate equal to twice ω_2. Instead, we sample Green's function at two different rates to evaluate ω_2 and then ω_1. Due to frequency aliasing, the order of the sampling is important. Choosing a low sampling rate to accurately evaluate the low frequency ω_1 may result in sampling below the nyquist rate of ω_2, the high frequency signal. For a given sampling rate ω_s, the alias frequency
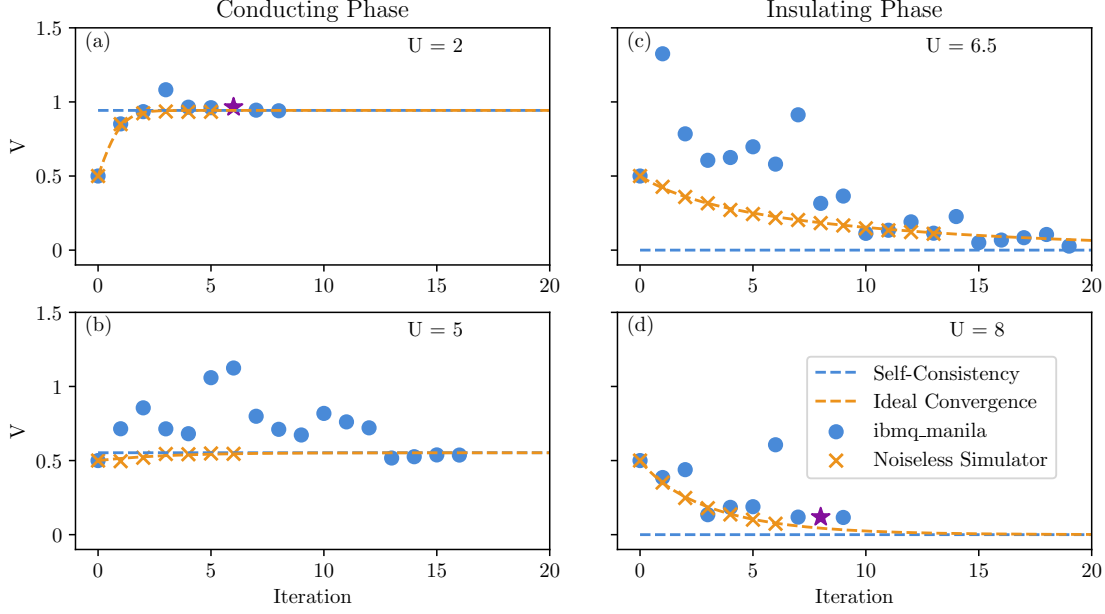
FIG. 5: DMFT step convergence behavior above (a/b) and below (c/d) critical $U_c = 6$. Despite error in the updated V, all values of converge to within the tolerance, with the except of U = 6.5 which terminates after no peaks near $\omega = 0$ were located. The starred points for U=2 and U=8 correspond to the Green's function evaluations plotted in figure 4 (a) and (b), respectively.

ω_a can be calculated from the true signal frequency ω using the following simple formula [41].

$$\omega_a = \left| \omega - \omega_s \times \text{NINT} \left(\frac{\omega}{\omega_s} \right) \right|, \tag{18}$$

where $\text{NINT}(x) \equiv \lceil \lfloor 2x \rfloor / 2 \rceil$ is the (round-half-up) nearest integer to x. Thus, we evaluate ω_2 first so the high frequency aliased signal appearing in the low frequency sampling regime can be discarded.

Figure 4 shows the evaluation of $iG(t)$ in the ideal case in orange (i/ii upper) and the results from high frequency sampling for ω_2 in purple (i, lower) and ω_1 in blue (ii, lower). In each case, t_H and t_L are sets of at 150 values for time and are chosen with sampling frequencies between three and ten times greater the than the frequency of ω_2 and ω_1 determined in the previous iteration of the DMFT loop (in both cases above the nyquist rate).

To prevent erroneous updates of the loop when an incorrect peak is found due to noise, only the frequency region around an expected peak, as determined by the previous ω_1 and ω_2 calculation, is searched for peaks. Additionally, each evaluation $iG(t_L)$ and $iG(t_H)$ has a condition to fail for not enough (0) or too many (>4) prominent frequency peaks present in the DFT, as determined by an adaptive height criteria based on the average and standard deviation of the absolute value of the DFT amplitudes. In the case a condition fails, the particular high frequency or low frequency calculation is rerun until the condition passes and $\mathcal{Z}$ is computed. The loop is iterated until two sequential results of V are within a tolerance, in our case chosen to be 0.02. The exception is the convergence for $U = 6.5$, in which a prominent peak for ω_1 was not found after 3 attempts and the loop was terminated. This corresponds to failing to find a frequency with amplitude 10^{-4} within the signal-to-noise ratio of the quantum computer. The removal of the dependence on amplitude in computing of $\mathcal{Z}$ is essential to the success of the DMFT calculation. The final results of the Green's function evaluation, before normalization, leads to amplitudes between 5 and 15 times lower than in the ideal case, and in general relative signal amplitude is not reliably preserved in the final computation.

V. RESULTS

Despite significant noise, the quasi-particle and Hubbard band frequencies are preserved in the final discrete Fourier transform of the Green's function evaluation, allowing for reasonable updates to the DMFT loop, as shown in figure 5.
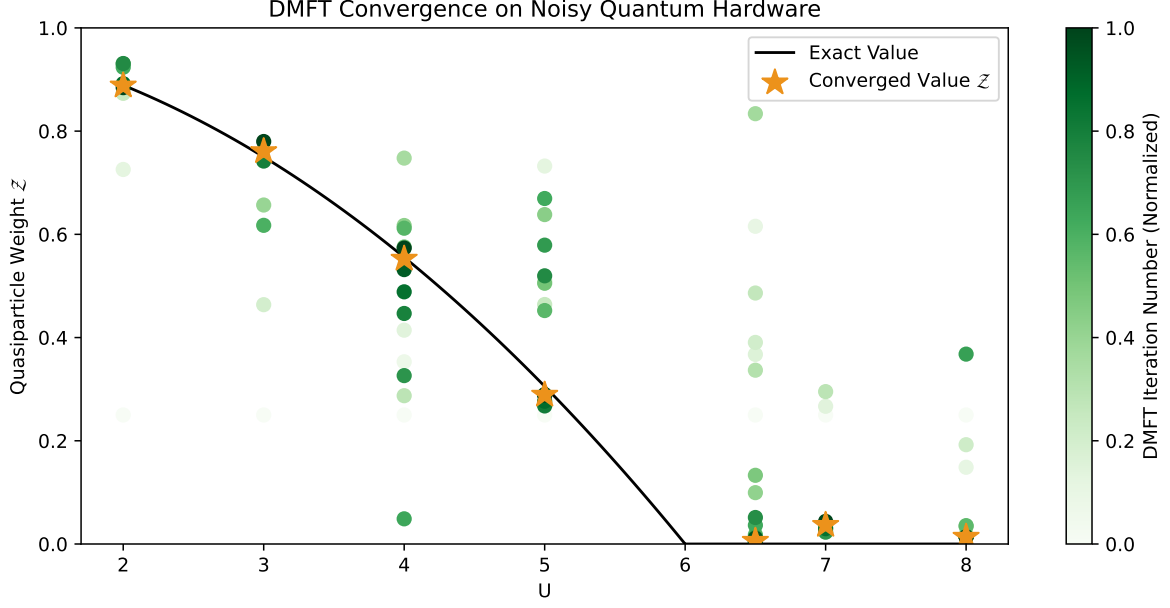
FIG. 6: DMFT phase diagram computed on a quantum computer. The solid black line corresponds to the exact value of self-consistency Eq. Eq. (19), and increasing values of the iteration correspond to steps later in the DMFT loop. We have omitted from the plot values of $\mathcal{Z}$ which are above 1. The gap in convergence around $U_c = 6$ corresponds to the region where the critical slowing means computing the DMFT loop is cost-prohibitive.

The analytical convergence [42], which is interpolated to serve as a guideline, is compared to the behavior of the convergence of the identical algorithm on a noiseless simulator and the results on quantum hardware. In the insulating phase, even on the noiseless simulator, our algorithm fails to converge exactly to zero for ω_1 due to the vanishing amplitude of α_1. Despite significant deviations from the ideal convergence behavior and sequential updates, the convergence on the quantum hardware trends toward self-consistency. In the case of $U = 6.5$, these deviations serve to increase the rate of convergence, but generally the deviations prevent ideal, sequential convergence in spite of the significant filtering and error mitigation.

Figure 6 shows the phase diagram of the quasi-particle weight $\mathcal{Z}_{\mathrm{noisy}}$ produced on quantum hardware, plotted against the exact self-consistent solutions for $\mathcal{Z}_{\mathrm{exact}}$ [33]

$$\mathcal{Z}_{\mathrm{exact}} = \begin{cases} \dfrac{36 - U^2}{36}, \ U < U_c = 6 \\ \\ 0, \ U \geq 6 \end{cases} \tag{19}$$

For all values of U, the initial value of $V = 0.5$ is used and the color gradient shows the convergence toward the final value V_{noisy}, which is taken to be the average of the final two steps in the loop. For $U < U_c$, the convergence is within the tolerance $|V_{\mathrm{noisy}} - V_{\mathrm{ideal}}| < 0.02$ at self-consistency for V. For $U > U_C$, α_1 and ω_1 both vanish to zero, requiring both very long time simulation and a very good signal-to-noise ratio in the results to determine convergence. $\mathcal{Z}$ instead converges to above zero but still clearly shows the phase transition. In this regime, the fast-forwarding allowed by Cartan decomposition is essential to appropriately study the dynamics over very long times. Results for U near U_c are omitted, as critical slowing prevents convergence within a reasonable number of iteration steps. The CNOT error and coherence time values for *ibmq_ manila* can be found in appendix D.

VI.   CONCLUSION

Here, we have implemented a two-site DMFT calculation on current generation superconducting quantum hardware with linear CNOT connectivity. Compared to previous methods using Trotter simulation to converge in the insulating

phase and variational methods to converge in the conducting phase, our work is the first general implementation to compute the entire DMFT phase diagram [8, 9]. We find that the bottlenecks in the calculation are the noise in the quantum computer and slow convergence near the transition point. To circumvent these issues we introduced a variety of optimization and error mitigation methods including randomized Cartan solutions in the time evolution, measurement error mitigation, analysis of alias signals in the DFT, and post selection of data. The post selection of data includes enforcement of particle number and total spin conservation since the Hamiltonian under consideration cannot create/destroy particles or flip the spin of particles.

Cartan decomposition as a means of fast-forwarding time evolution serves to preserve frequency information despite significant noisy operation in the quantum computer, as demonstrated in this work. Although the algorithm used scales poorly with the number of lattice sites in models of interacting fermions, in such a four-qubit simulation the depth of the algorithm, although significantly longer than a single Trotter step, does not introduce additional numerical errors to the already noisy simulation results and provides access to simulations over much longer time scales than approximations with error scaling in time. Thus, for calculations which depend on oscillation frequencies, such as the DMFT and other embedding problems, this and other fast-forwarding algorithms may prove valuable in in the near term, especially when tailored for hardware connectivity.

DATA AVAILABILITY

The data that support the findings of this study are available from the authors upon request.

Appendix A: Jordan-Wigner transformation

For digital quantum simulation of fermionic systems, we generally map the fermionic algebra of fermion creation and annihilation operators to the qubit algebra of Pauli strings $\bigotimes_{l=0}^{n} \hat{\sigma}_l^{a_l}$ ($a_l \in \{x, y, z, 0\}$) that are Kronecker tensor products of the Pauli matrices $\hat{\sigma}^x = X = \left(\begin{smallmatrix} 0 & 1 \\ 1 & 0 \end{smallmatrix}\right)$, $\hat{\sigma}^y = Y = \left(\begin{smallmatrix} 0 & -i \\ i & 0 \end{smallmatrix}\right)$, and $\hat{\sigma}^z = Z = \left(\begin{smallmatrix} 1 & 0 \\ 0 & -1 \end{smallmatrix}\right)$ and the identity matrix $\hat{\sigma}^0 = I = \left(\begin{smallmatrix} 1 & 0 \\ 0 & 1 \end{smallmatrix}\right)$. The Jordan-Wigner transformation [43] used in this work is one such method. The Pauli strings for N-qubit systems are the Kronecker tensor products of N Pauli or identity matrices. We define $Z_i = I^{\otimes(i-1)} \otimes Z \otimes I^{\otimes(N-i)}$ for the type of Pauli strings acting on only a single qubit. The standard procedure follows an algorithm to map the fermionic basis states to the computational basis spanned by a sequence of qubits and the fermionic operators to the sum of Pauli string operators on these qubits. This is given as follows.

1. Map fermionic states to qubit states. We employ a mapping where the spin-orbitals $|i\sigma\rangle$ for the same spin but different sites are grouped together $|0\uparrow, 1\uparrow, \cdots, 0\downarrow, 1\downarrow, \cdots\rangle$. Occupied states are $|1\rangle$ in the computational basis, and unoccupied states are $|0\rangle$.

2. Apply $\hat{c} \rightarrow \hat{\sigma}_+ = \frac{1}{2}(X + iY)$ and $\hat{c}^\dagger \rightarrow \hat{\sigma}_- = \frac{1}{2}(X - iY)$. From these two identities, we also get $\hat{n} \rightarrow \frac{1}{2}(I - Z)$ and $\hat{h} \rightarrow \frac{1}{2}(I + Z)$.

3. To maintain canonical anti-commutation relations for fermion operators $\left\{\hat{c}_{j\sigma}, \hat{c}_{j'\sigma'}^\dagger\right\} = \delta_{jj'}\delta_{\sigma\sigma'}$ and $\left\{\hat{c}_{j\sigma}, \hat{c}_{j'\sigma'}\right\} =$

$\left\{\hat{c}_{j\sigma}^{\dagger}, \hat{c}_{j'\sigma'}^{\dagger}\right\} = 0$, map the indexed fermionic operators (site index $0 \leq j \leq N_b$) to the corresponding qubit operators as follows.

$$\hat{c}_{j\uparrow} = \frac{1}{2}Z_1 \cdots Z_{j-1}(X_j + iY_j), \qquad\qquad \hat{c}_{j\uparrow}^{\dagger} = \frac{1}{2}Z_1 \cdots Z_{j-1}(X_j - iY_j),$$

$$\hat{c}_{j\downarrow} = \frac{1}{2}Z_1 \cdots Z_{N_b+j}(X_{N_b+1+j} + iY_{N_b+1+j}), \quad \hat{c}_{j\downarrow}^{\dagger} = \frac{1}{2}Z_1 \cdots Z_{N_b+j}(X_{N_b+1+j} - iY_{N_b+1+j}),$$

$$\hat{n}_{0\uparrow} = \frac{1}{2}(I_0 - Z_0), \qquad\qquad\qquad \hat{n}_{0\downarrow} = \frac{1}{2}(I_{N_b+1} - Z_{N_b+1}).$$

In the above, $Z_j \cdots Z_{j'} = \prod_{k=j}^{j'} Z_k$ for $j' \geq j$ and $Z_j \cdots Z_{j'} = 1$ for $j' < j$.

Applying the above steps to the AIM Hamiltonian yields

$$\begin{aligned}
\hat{H}_{\text{AIM}} = \sum_{i=1}^{N_b} \frac{V_i}{2}\big(&X_0 Z_1 \cdots Z_{i-1} X_i + Y_0 Z_1 \cdots Z_{i-1} Y_i \\
&+ X_{N_b+1} Z_{N_b+2} \cdots Z_{N_b+i} X_{N_b+1+i} + Y_{N_b+1} Z_{N_b+2} \cdots Z_{N_b+i} Y_{N_b+1+i}\big) \\
&+ \frac{U}{4}(Z_0 Z_{N_b+1} - Z_0 - Z_{N_b+1}) + \sum_{i=0}^{N_b} \frac{\epsilon_i - \mu}{2}(Z_i + Z_{N_b+1+i}).
\end{aligned} \tag{A1}$$

We have dropped a constant term $\frac{U}{4}I_0 I_{N_b+1} = \frac{U}{4}$ from the above Hamiltonian since a constant energy shift does not affect the dynamics of a system.

The Hamiltonian simplifies in the two-site case (one impurity site and $N_b = 1$ bath site). Further, due to particle-hole symmetry of a half-filling (total two particles) ground state we will consider, additional constraints on ϵ_0 and ϵ_1 are as follows: the impurity on-site energy $\epsilon_0 = 0$, so $\epsilon_0 - \mu = -\mu = -\frac{U}{2}$; ϵ_1 must satisfy a self-consistency condition in which the occupation of the impurity site is defined by to the occupation of the Hubbard lattice, which results in $\epsilon_1 - \mu = 0$ [33, 34]. Therefore, the simplified two-site $\hat{H}_{\text{AIM}}$ with a half-filling ground state is then given by

$$\hat{H}_{\text{AIM}} = \frac{V}{2}(X_0 X_1 + Y_0 Y_1 + X_2 X_3 + Y_2 Y_3) + \frac{U}{4}Z_0 Z_2. \tag{A2}$$

Appendix B: Green's function evaluation

The retarded impurity Green's function is given by

$$G_{\text{imp}}^{\text{R}}(t) = -i\theta(t)\left\langle \psi_0 \left| \left\{\hat{c}_0(t), \hat{c}_0^{\dagger}\right\} \right| \psi_0 \right\rangle = -i\theta(t)\left\langle \psi_0 \left| \hat{c}_0(t)\hat{c}_0^{\dagger} + \hat{c}_0^{\dagger}\hat{c}_0(t) \right| \psi_0 \right\rangle, \tag{B1}$$

where $\hat{c}_0(t) = e^{i\hat{H}_{\text{AIM}}t}\hat{c}_0 e^{-i\hat{H}_{\text{AIM}}t}$, $\hat{c}_0^{\dagger}(t) = e^{i\hat{H}_{\text{AIM}}t}\hat{c}_0^{\dagger}e^{-i\hat{H}_{\text{AIM}}t}$, $|\psi_0\rangle$ is the ground state of the impurity Hamiltonian $\hat{H}_{\text{AIM}}$, $\theta(t)$.

Denote $U(t) = e^{-i\hat{H}t}$ and apply the Jordan-Wigner transform to these terms, we have

$$\begin{aligned}
G^<(t) &= i\left\langle \psi_0 \left| \frac{1}{2}(X_0 - iY_0)U^{\dagger}(t)\frac{1}{2}(X_0 + iY_0)U(t) \right| \psi_0 \right\rangle \\
&= \frac{i}{4}\left[\langle X_0 U^{\dagger}(t)X_0 U(t)\rangle + i\langle X_0 U^{\dagger}(t)Y_0 U(t)\rangle - i\langle Y_0 U^{\dagger}(t)X_0 U(t)\rangle + \langle Y_0 U^{\dagger}(t)Y_0 U(t)\rangle\right] \\
G^>(t) &= -i\left\langle \psi_0 \left| U^{\dagger}(t)\frac{1}{2}(X_0 + iY_0)U(t)\frac{1}{2}(X_0 - iY_0) \right| \psi_0 \right\rangle \\
&= \frac{-i}{4}\left[\langle U^{\dagger}(t)X_0 U(t)X_0\rangle + i\langle U^{\dagger}(t)Y_0 U(t)X_0\rangle - i\langle U^{\dagger}(t)X_0 U(t)Y_0\rangle + \langle U^{\dagger}(t)Y_0 U(t)Y_0\rangle\right].
\end{aligned}$$

Measuring the 8 terms in function $4iG_{\text{imp}}^R(t > 0) = 4i[G^>(t) - G^<(t)] = \langle X_0(t)X_0\rangle + i\langle Y_0(t)X_0\rangle - i\langle X_0(t)Y_0\rangle + \langle Y_0(t)Y_0\rangle + \langle X_0 X_0(t)\rangle + i\langle X_0 Y_0(t)\rangle - i\langle Y_0 X_0(t)\rangle + \langle Y_0 Y_0(t)\rangle$ would require 16 total circuits: two circuits per term for the real and imaginary components, respectively. We reduce the evaluation to only two measurement circuits for real

component of the two terms $\langle X_0(t)X_0\rangle$ and $\langle Y_0(t)Y_0\rangle$. The simplification follows

$$
\begin{aligned}
&4iG_{\mathrm{imp}}^{\mathrm{R}}(t>0)\\
&=4i[G^>(t)-G^<(t)]\\
&=[\langle X_0(t)X_0\rangle+\langle X_0X_0(t)\rangle] &&+i[\langle Y_0(t)X_0\rangle+\langle X_0Y_0(t)\rangle] &&-i[\langle X_0(t)Y_0\rangle+\langle Y_0X_0(t)\rangle] &&+[\langle Y_0(t)Y_0\rangle+\langle Y_0Y_0(t)\rangle]\\
&=[\langle X_0(t)X_0\rangle+\langle X_0(t)X_0\rangle^*] &&+i[\langle Y_0(t)X_0\rangle+\langle Y_0(t)X_0\rangle^*] &&-i[\langle X_0(t)Y_0\rangle+\langle X_0(t)Y_0\rangle^*] &&+[\langle Y_0(t)Y_0\rangle+\langle Y_0(t)Y_0\rangle^*]\\
&=2\,\mathrm{Re}\,\langle X_0(t)X_0\rangle &&+2i\,\mathrm{Re}\,\langle Y_0(t)X_0\rangle &&-2i\,\mathrm{Re}\,\langle X_0(t)Y_0\rangle &&+2\,\mathrm{Re}\,\langle Y_0(t)Y_0\rangle .
\end{aligned}
$$

Since at half-filling, due to particle-hole symmetry, the imaginary component of $iG_{\mathrm{imp}}^{\mathrm{R}}(t)$ is zero, we only need to measure the first and last term in the above: the real components $\mathrm{Re}\,\langle X_0(t)X_0\rangle$ and $\mathrm{Re}\,\langle Y_0(t)Y_0\rangle$.

Appendix C: Singular behavior of self-energy and its derivative at zero frequency

We drop the impurity "imp" subscript below for simplicity. Green's function in the time domain has the form

$$
iG(t>0)=\alpha_1 e^{i\omega_1 t}+\alpha_1 e^{-i\omega_1 t}+\alpha_2 e^{i\omega_2 t}+\alpha_2 e^{-i\omega_2 t}=2\alpha_1\cos(\omega_1 t)+2\alpha_2\cos(\omega_2 t), \tag{C1}
$$

To extract the poles $\omega=\omega_{1,2}$ and pole strength $\alpha_{1,2}$ of the retarded interacting impurity Green's function, initially take the analytic Fourier transform

$$
G(\omega)=\frac{\alpha_1}{\omega-\omega_1}+\frac{\alpha_1}{\omega+\omega_1}+\frac{\alpha_2}{\omega-\omega_2}+\frac{\alpha_2}{\omega+\omega_2}. \tag{C2}
$$

From the definitions of the self-energy and it's derivatives, we find:

$$
\Sigma(\omega)=\frac{1}{G^{(0)}(\omega)}-\frac{1}{G(\omega)}, \tag{C3}
$$

$$
\frac{d\Sigma(\omega)}{d\omega}=-\frac{dG^{(0)}(\omega)/d\omega}{[G^{(0)}(\omega)]^2}+\frac{dG(\omega)/d\omega}{[G(\omega)]^2}. \tag{C4}
$$

$$
G^{(0)}(\omega)=\frac{1/2}{\omega-V}+\frac{1/2}{\omega+V}, \tag{C5}
$$

$$
G^{(0)}(\omega)\Big|_{\omega=0}=1/(-2V)+1/(2V)=0.
$$

$$
\frac{dG^{(0)}(\omega)}{d\omega}=-\frac{1}{2(\omega-V)^2}-\frac{1}{2(\omega+V)^2}, \tag{C6}
$$

$$
\frac{dG(\omega)}{d\omega}=-\frac{\alpha_1}{(\omega-\omega_1)^2}-\frac{\alpha_1}{(\omega+\omega_1)^2}-\frac{\alpha_2}{(\omega-\omega_2)^2}-\frac{\alpha_2}{(\omega+\omega_2)^2}, \tag{C7}
$$

$$
\begin{aligned}
\frac{d\Sigma(\omega)}{d\omega}&=-\frac{dG^{(0)}(\omega)/d\omega}{G_0^2(\omega)}+\frac{dG(\omega)/d\omega}{G^2(\omega)}\\[2mm]
&=\frac{\dfrac{1/2}{(\omega-V)^2}+\dfrac{1/2}{(\omega+V)^2}}{\left(\dfrac{1/2}{\omega-V}+\dfrac{1/2}{\omega+V}\right)^2}-\frac{\dfrac{\alpha_1}{(\omega-\omega_1)^2}+\dfrac{\alpha_1}{(\omega+\omega_1)^2}+\dfrac{\alpha_2}{(\omega-\omega_2)^2}+\dfrac{\alpha_2}{(\omega+\omega_2)^2}}{\left(\dfrac{\alpha_1}{\omega-\omega_1}+\dfrac{\alpha_1}{\omega+\omega_1}+\dfrac{\alpha_2}{\omega-\omega_2}+\dfrac{\alpha_2}{\omega+\omega_2}\right)^2}\\[2mm]
&=\frac{\omega^2+V^2}{\omega^2}-\frac{\alpha_1(\omega^2-\omega_2^2)^2(\omega^2+\omega_1^2)+\alpha_2(\omega^2-\omega_1^2)^2(\omega^2+\omega_2^2)}{2\omega^2[\alpha_1(\omega^2-\omega_2^2)+\alpha_2(\omega^2-\omega_1^2)]^2}\\[2mm]
&=1+\frac{V^2}{\omega^2}-\frac{\alpha_1(\omega^2-\omega_2^2)^2+\alpha_2(\omega^2-\omega_1^2)^2}{2[\alpha_1(\omega^2-\omega_2^2)+\alpha_2(\omega^2-\omega_1^2)]^2}-\frac{\alpha_1(\omega^2-\omega_2^2)^2\omega_1^2+\alpha_2(\omega^2-\omega_1^2)^2\omega_2^2}{2\omega^2[\alpha_1(\omega^2-\omega_2^2)+\alpha_2(\omega^2-\omega_1^2)]^2}. \tag{C8}
\end{aligned}
$$

$$
\Sigma'(\omega)=-\frac{1}{\omega^2}\left\{\frac{\alpha_1(\omega^2-\omega_2^2)^2\omega_1^2+\alpha_2(\omega^2-\omega_1^2)^2\omega_2^2}{2[\alpha_1(\omega^2-\omega_2^2)+\alpha_2(\omega^2-\omega_1^2)]^2}-V^2\right\}+1-\frac{\alpha_1(\omega^2-\omega_2^2)^2+\alpha_2(\omega^2-\omega_1^2)^2}{2[\alpha_1(\omega^2-\omega_2^2)+\alpha_2(\omega^2-\omega_1^2)]^2} \tag{C9}
$$

$$
\equiv-\frac{1}{x}\left[\frac{f(x)}{g(x)}-V^2\right]+h(x). \tag{C10}
$$

In the last step, we have defined functions $f(x) = \alpha_1 (x - x_2)^2 x_1 + \alpha_2 (x - x_1)^2 x_2$, $g(x) = 2[\alpha_1 (x - x_2) + \alpha_2 (x - x_1)]^2$, and $h(x) = 1 - [\alpha_1 (x - x_2)^2 + \alpha_2 (x - x_1)^2]/g(x)$, where $x = \omega^2$, $x_1 = \omega_1^2$, and $x_2 = \omega_2^2$, for the discussion below. Before making any further simplification, we check the consistency of Eq. (C9).

- First check, for $U = 0$, $\alpha_1 = 1/2$, $\alpha_2 = 0$, $\omega_1 = V$. From Eqs. (C3) and Eq. (C2), we find $\Sigma(\omega) = 0$ and $\Sigma'(\omega) = \frac{\mathrm{d}\Sigma(\omega)}{\mathrm{d}\omega} = 0$. Plugging $\alpha_1 = 1/2$, $\alpha_2 = 0$, $\omega_1 = V$ into Eq. (C9), we also find $\Sigma'(\omega) = 0$.

- Second check, for $V = 0$ (the so-called atomic limit where the "atom" is the single impurity site), $\alpha_1 = 0$, $\alpha_2 = 1/2$, $\omega_1 = 0$ and $\omega_2 = U/2$. From Eqs. (C3) and Eq. (C2), we find $\Sigma(\omega) = (\frac{1}{\omega})^{-1} - (\frac{1}{2\omega - U} + \frac{1}{2\omega + U})^{-1} = \omega - \frac{4\omega^2 - U^2}{4\omega} = \frac{U^2}{4\omega}$ and $\Sigma'(\omega) = \frac{\mathrm{d}\Sigma(\omega)}{\mathrm{d}\omega} = -\frac{U^2}{4\omega^2}$. Plugging $\alpha_1 = 0$, $\alpha_2 = 1/2$, $\omega_2 = U/2$ into Eq. (C9), we also find $\Sigma'(\omega) = -\frac{\omega_2^2}{\omega^2} = -\frac{U^2}{4\omega^2}$.

Now we derive a more stable formula to calculate $\lim_{\omega \to 0} \frac{\mathrm{d}\Sigma(\omega)}{\mathrm{d}\omega} \equiv \Sigma'(0)$. First, $h(x)|_{x=\omega^2=0}$ is finite because if the denominator of the second term in $h(x)$ is zero at $x = \omega^2 = 0$, this implies that $\alpha_1 \omega_2^2 + \alpha_2 \omega_1^2 = 0$, which is impossible since α_1, α_2, ω_1, $\omega_2 \geq 0$, $\alpha_1 + \alpha_2 > 0$, and $\omega_1 + \omega_2 > 0$. Therefore, the first term of $\Sigma'(\omega)$, $-\frac{1}{x}\left[\frac{f(x)}{g(x)} - V^2\right]$, must also be finite as $x = \omega^2 \to 0$. This is only possible if $\frac{f(x)}{g(x)} - V^2\Big|_{x=0} = 0$, which gives

$$\frac{f(x)}{g(x)}\Big|_{x=0} = \frac{f(0)}{g(0)} = \frac{\alpha_1 x_2^2 x_1 + \alpha_2 x_1^2 x_2}{2(\alpha_1 x_2 + \alpha_2 x_1)^2} = \frac{x_1 x_2 (\alpha_1 x_2 + \alpha_2 x_1)}{2(\alpha_1 x_2 + \alpha_2 x_1)^2} = \frac{x_1 x_2}{2(\alpha_1 x_2 + \alpha_2 x_1)} = V^2. \tag{C11}$$

Therefore, we can evaluate the $x \to 0$ limit of the first term $-\frac{1}{x}\left[\frac{f(x)}{g(x)} - V^2\right]$ with L'Hôpital's rule as follows.

$$\lim_{x \to 0} -\frac{1}{x}\left[\frac{f(x)}{g(x)} - V^2\right] = \lim_{x \to 0} \frac{g(x)V^2 - f(x)}{xg(x)} = \lim_{x \to 0} \frac{\mathrm{d}[g(x)V^2 - f(x)]/\mathrm{d}x}{\mathrm{d}[xg(x)]/\mathrm{d}x}$$

$$= \lim_{x \to 0} \frac{g'(x)V^2 - f'(x)}{g(x) + xg'(x)} = \frac{g'(0)V^2 - f'(0)}{g(0)}. \tag{C12}$$

$$f(x) = \alpha_1 (x - x_2)^2 x_1 + \alpha_2 (x - x_1)^2 x_2,$$
$$f'(x) = 2\alpha_1 (x - x_2) x_1 + 2\alpha_2 (x - x_1) x_2,$$
$$f'(0) = -2x_1 x_2 (\alpha_1 + \alpha_2) = -4V^2 (\alpha_1 x_2 + \alpha_2 x_1)(\alpha_1 + \alpha_2). \quad \text{[see Eq. (C11)]}$$
$$g(x) = 2[\alpha_1 (x - x_2) + \alpha_2 (x - x_1)]^2,$$
$$g'(x) = 4[\alpha_1 (x - x_2) + \alpha_2 (x - x_1)](\alpha_1 + \alpha_2),$$
$$g'(0) = -4(\alpha_1 x_2 + \alpha_2 x_1)(\alpha_1 + \alpha_2).$$

$$\therefore \lim_{x \to 0} -\frac{1}{x}\left[\frac{f(x)}{g(x)} - V^2\right] = \frac{g'(0)V^2 - f'(0)}{g(0)}$$

$$= \frac{-4V^2 (\alpha_1 x_2 + \alpha_2 x_1)(\alpha_1 + \alpha_2) + 4V^2 (\alpha_1 x_2 + \alpha_2 x_1)(\alpha_1 + \alpha_2)}{g(0)} = 0. \tag{C13}$$

Since the first term of $\Sigma'(\omega)$, Eq. (C13), is zero, we find

$$\frac{\mathrm{d}\Sigma(\omega)}{\mathrm{d}\omega}\Big|_{\omega=0} = h(0) = 1 - \frac{\alpha_1 x_2^2 + \alpha_2 x_1^2}{2(\alpha_1 x_2 + \alpha_2 x_1)^2}, \tag{C14}$$

$$\mathcal{Z} = 1 \Big/ \left[1 - \frac{\mathrm{d}\mathrm{Re}\Sigma(\omega)}{\mathrm{d}\omega}\right]_{\omega=0} = \frac{2(\alpha_1 x_2 + \alpha_2 x_1)^2}{\alpha_1 x_2^2 + \alpha_2 x_1^2}, \tag{C15}$$

$$x_1 = \omega_1^2, \ x_2 = \omega_2^2.$$

Eqs. (C14) and (C15) are more stable and robust against numerical or (quantum) simulation error comparing to the analytical formula Eq. (C9) for the derivative $\frac{\mathrm{d}\Sigma(\omega)}{\mathrm{d}\omega}$ or a numerical implementation:

$$\frac{\mathrm{d}\Sigma(\omega)}{\mathrm{d}\omega} \approx \frac{[1/G^{(0)}(\Delta\omega) - 1/G(\Delta\omega)] - [1/G^{(0)}(-\Delta\omega) - 1/G(-\Delta\omega)]}{2\Delta\omega}.$$

The stability comes from the removal of the first term in Eq. (C9) which is mathematically singular if the condition

Eq. (C11) is not satisfied exactly. Numerically, adding a small imaginary part to the frequency $\omega \to \omega + i\delta$ or using a finite step size $\Delta\omega$ in the derivative calculation might reduce the divergence but this is less stable than using Eqs. (C14) and (C15).

Last, we can strictly enforce the two conditions $\alpha_1 + \alpha_2 = \frac{1}{2}$ and Eq. (C11) $\frac{\alpha_1}{x_1} + \frac{\alpha_2}{x_2} = \frac{1}{2V^2}$ in Eqs. (C14) and (C15) to further improve accuracy. The two conditions can be enforced during the parameter fitting step, but this is not required since in the following equations, we use $\alpha_1 + \alpha_2 = \frac{1}{2}$ and $\frac{\alpha_1}{x_1} + \frac{\alpha_2}{x_2} = \frac{1}{2V^2}$ to eliminate the less accurate fitting parameters ω_1 and α_1 when V is small or $V \to 0$ in the DMFT self-consistent loop calculation for insulating phase. In this case, $\alpha_1 \to 0$, $\alpha_2 \to \frac{1}{2}$, $\omega_2 \to \frac{U}{2}$, $x_2 \to \omega_2^2 \to \frac{U^2}{4}$, so $\frac{\alpha_2}{x_2} \to \frac{2}{U^2}$ and $\frac{\alpha_1}{x_1} \to \frac{1}{2V^2} - \frac{2}{U^2}$.

$$
\begin{aligned}
\mathcal{Z} &= \frac{2\left(\alpha_1 x_2 + \alpha_2 x_1\right)^2}{\alpha_1 x_2^2 + \alpha_2 x_1^2} = \frac{2\left(\frac{\alpha_1}{x_1} + \frac{\alpha_2}{x_2}\right)^2}{\frac{\alpha_1}{x_1^2} + \frac{\alpha_2}{x_2^2}} \\
&= \frac{\frac{1}{2V^4}}{\frac{\alpha_1^2}{x_1^2}\frac{1}{\alpha_1} + \frac{\alpha_2}{x_2^2}} \xrightarrow{V\to 0} \frac{2\alpha_1}{4V^4\left(\frac{1}{2V^2} - \frac{2}{U^2} + o(1)\right)^2 + 4V^4 \alpha_1 \frac{\alpha_2}{x_2^2}} \\
&\xrightarrow{V\to 0} \frac{2\alpha_1}{4V^4\left(\frac{1}{4V^4} - \frac{2}{V^2 U^2} + O(1)\right) + O(V^4)} \\
&= 2\alpha_1\left(1 + \frac{8V^2}{U^2} + O(V^4)\right) = (1 - 2\alpha_2)\left(1 + \frac{8V^2}{U^2} + O(V^4)\right).
\end{aligned}
\tag{C16}
$$

The final Eq. (C16) is equivalent to the $\mathcal{Z}$ obtained from integrating the spectral function $\int_{-\omega_1^+}^{\omega_1^+} d\omega\, A(\omega) = \int_{-\omega_1^+}^{\omega_1^+} d\omega\, [\alpha_1 \delta(\omega - \omega_1) + \alpha_1 \delta(\omega + \omega_1)] = 2\alpha_1$.

Alternatively, we can use the two conditions

$$
\alpha_1 + \alpha_2 = \frac{1}{2}
\tag{C17a}
$$

$$
x_2 \alpha_1 + x_1 \alpha_2 = \frac{x_1 x_2}{2V^2}
\tag{C17b}
$$

to solve for α_1 and α_2 in terms of x_1, x_2, and V, and then eliminate them from the Eq. (C15). The final result is

$$
\mathcal{Z} = \frac{x_1 x_2}{V^2(x_1 + x_2 - V^2)} = \frac{\omega_1^2 \omega_2^2}{V^2(\omega_1^2 + \omega_2^2 - V^2)}.
\tag{C18}
$$

In practice, for $U \lesssim U_c$, the following formula using only the parameters $(\alpha_1/\alpha_2, \omega_2, V)$ might be more suitable to calculate $\mathcal{Z}$ from self-energy derivative:

$$
\mathcal{Z} = \frac{\alpha_1/\alpha_2}{(\alpha_1/\alpha_2) + (1 - V^2/\omega_2^2)^2}.
\tag{C19}
$$

Appendix D: Quantum Hardware

The quantum hardware used in this work was *ibmq_manila*, a 5 qubit superconducting device which is publicly available through the IBM Quantum Experience. The experiment parameters are designed around the open access quantum job submission limits of 5 sets of 75 circuit evaluations of 8,192 shots each. Thus, we used two distinct solutions to the Cartan decomposition which combine to a total shot count of 16,000 at each of 150 time step evaluations. The first set was reserved for just in time measurement error mitigation circuits, of which there are 32 circuits preparing each of the 2^5 computational basis states. Assuming a correct evaluation, each DMFT Loop requires approximately 36 minutes to execute on the IBM backend, including the Measurement Error Mitigation circuits. In practice, the update failure condition results in repeated calculations and subsequently increased run-times for each V update. Tables I and II show the qubit coherence times and the entangling gate properties, respectively. The ancilla qubit was placed at index 0. Calibration data pulled from the Qiskit API, and averaged by taking the calibration data at 4 points each day between October 10$^{\text{th}}$ 2021 and November 10$^{\text{th}}$ 2021 [38].

Qubit Number	T1 (μs)	T2 (μs)
0 (Ancilla)	146.18 ± 29.78	94.38 ± 18.50
1	204.64 ± 47.57	83.02 ± 15.18
2	148.79 ± 26.79	24.30 ± 2.55
3	157.19 ± 36.33	63.64 ± 7.83
4	128.96 ± 24.11	42.78 ± 2.57

TABLE I: Average T1 and T2 coherence times for *ibmq_ manila*, averaged over the period of time in which runs were executed.

Connection	CNOT Fidelity	Gate Timing (ns)
0-1	0.0070 ± 0.0012	295.11 ± 17.78
1-2	0.0099 ± 0.0017	487.11 ± 17.78
2-3	0.0071 ± 0.00080	373.33 ± 17.78
3-4	0.0076 ± 0.0016	316.44 ± 17.78

TABLE II: Average CNOT fidelity and gate timings on *ibmq_ manila*.

[1] P. W. Shor, Polynomial-time algorithms for prime factorization and discrete logarithms on a quantum computer, SIAM Journal on Computing **26**, 1484–1509 (1997).
[2] B. Bauer, D. Wecker, A. J. Millis, M. B. Hastings, and M. Troyer, Hybrid quantum-classical approach to correlated materials, Physical Review X **6**, 1 (2016).
[3] I. D. Kivlichan, J. McClean, N. Wiebe, C. Gidney, A. Aspuru-Guzik, G. K. L. Chan, and R. Babbush, Quantum Simulation of Electronic Structure with Linear Depth and Connectivity, Physical Review Letters **120**, 110501 (2018).
[4] Z. Jiang, K. J. Sung, K. Kechedzhi, V. N. Smelyanskiy, and S. Boixo, Quantum Algorithms to Simulate Many-Body Physics of Correlated Fermions, Physical Review Applied **9**, 44036 (2018).
[5] D. Wecker, M. B. Hastings, N. Wiebe, B. K. Clark, C. Nayak, and M. Troyer, Solving strongly correlated electron models on a quantum computer, Physical Review A - Atomic, Molecular, and Optical Physics **92**, 1 (2015).
[6] C. Cade, L. Mineh, A. Montanaro, and S. Stanisic, Strategies for solving the fermi-hubbard model on near-term quantum computers, Physical Review B **102**, 235122 (2020).
[7] N. M. Linke, S. Johri, C. Figgatt, K. A. Landsman, A. Y. Matsuura, and C. Monroe, Measuring the Rényi entropy of a two-site Fermi-Hubbard model on a trapped ion quantum computer, Physical Review A **98**, 10.1103/PhysRevA.98.052334 (2018).
[8] I. Rungger, N. Fitzpatrick, H. Chen, C. H. Alderete, H. Apel, A. Cowtan, A. Patterson, D. M. Ramo, Y. Zhu, N. H. Nguyen, E. Grant, S. Chretien, L. Wossnig, N. M. Linke, and R. Duncan, Dynamical mean field theory algorithm and experiment on quantum computers (2019), arXiv:arXiv:1910.04735.
[9] T. Keen, T. Maier, S. Johnston, and P. Lougovski, Quantum-classical simulation of two-site dynamical mean-field theory on noisy quantum hardware, Quantum Science and Technology **5**, 035001 (2020).
[10] A. Liebsch and H. Ishida, Temperature and bath size in exact diagonalization dynamical mean field theory, Journal of Physics Condensed Matter **24**, 10.1088/0953-8984/24/5/053201 (2012).
[11] E. Gull, A. J. Millis, A. I. Lichtenstein, A. N. Rubtsov, M. Troyer, and P. Werner, Continuous-time monte carlo methods for quantum impurity models, Rev. Mod. Phys. **83**, 349 (2011).
[12] F. A. Wolf, I. P. McCulloch, and U. Schollwöck, Solving nonequilibrium dynamical mean-field theory using matrix product states, Phys. Rev. B **90**, 235131 (2014).
[13] M. Troyer and U.-J. Wiese, Computational complexity and fundamental limitations to fermionic quantum monte carlo simulations, Physical Review Letters **94**, 10.1103/physrevlett.94.170201 (2005).
[14] B. Jaderberg, A. Agarwal, K. Leonhardt, M. Kiffner, and D. Jaksch, Minimum hardware requirements for hybrid quantum–classical dmft, Quantum Science and Technology **5**, 034015 (2020).
[15] E. Kökcü, T. Steckmann, J. K. Freericks, E. F. Dumitrescu, and A. F. Kemper, Fixed depth Hamiltonian simulation via Cartan decomposition, arXiv:2104.00728 [cond-mat, physics:quant-ph] (2021).
[16] N. F. MOTT, Metal-insulator transition, Rev. Mod. Phys. **40**, 677 (1968).
[17] M. Imada, A. Fujimori, and Y. Tokura, Metal-insulator transitions, Rev. Mod. Phys. **70**, 1039 (1998).
[18] A. Georges and G. Kotliar, Hubbard model in infinite dimensions, Phys. Rev. B **45**, 6479 (1992).
[19] S. R. White, D. J. Scalapino, R. L. Sugar, E. Y. Loh, J. E. Gubernatis, and R. T. Scalettar, Numerical study of the two-dimensional hubbard model, Phys. Rev. B **40**, 506 (1989).

[20] B.-X. Zheng, C.-M. Chung, P. Corboz, G. Ehlers, M.-P. Qin, R. M. Noack, H. Shi, S. R. White, S. Zhang, and G. K.-L. Chan, Stripe order in the underdoped region of the two-dimensional hubbard model, Science **358**, 1155 (2017).

[21] E. W. Huang, C. B. Mendl, H.-C. Jiang, B. Moritz, and T. P. Devereaux, Stripe order from the perspective of the hubbard model, npj Quantum Materials **3**, 22 (2018).

[22] E. W. Huang, R. Sheppard, B. Moritz, and T. P. Devereaux, Strange metallicity in the doped hubbard model, Science **366**, 987 (2019).

[23] E. Gull, O. Parcollet, and A. J. Millis, Superconductivity and the pseudogap in the two-dimensional hubbard model, Phys. Rev. Lett. **110**, 216405 (2013).

[24] X. Chen, J. P. F. LeBlanc, and E. Gull, Superconducting fluctuations in the normal state of the two-dimensional hubbard model, Phys. Rev. Lett. **115**, 116402 (2015).

[25] T. A. Maier, M. Jarrell, T. C. Schulthess, P. R. C. Kent, and J. B. White, Systematic study of d-wave superconductivity in the 2d repulsive hubbard model, Phys. Rev. Lett. **95**, 237001 (2005).

[26] J. Hubbard, Electron correlations in narrow energy bands, Proceedings of the Royal Society of London. Series A. Mathematical and Physical Sciences **276**, 238 (1963).

[27] D. Wecker, M. B. Hastings, and M. Troyer, Progress towards practical quantum variational algorithms, Physical Review A - Atomic, Molecular, and Optical Physics **92**, 1 (2015).

[28] J.-M. Reiner, F. Wilhelm-Mauch, G. Schön, and M. Marthaler, Finding the ground state of the Hubbard model by variational methods on a quantum computer with gate errors, Quantum Science and Technology **4**, 035005 (2019).

[29] I. D. Kivlichan, C. Gidney, D. W. Berry, N. Wiebe, J. McClean, W. Sun, Z. Jiang, N. Rubin, A. Fowler, A. Aspuru-Guzik, H. Neven, and R. Babbush, Improved Fault-Tolerant Quantum Simulation of Condensed-Phase Correlated Electrons via Trotterization, Quantum **4**, 296 (2020).

[30] D. Wecker, M. B. Hastings, N. Wiebe, B. K. Clark, C. Nayak, and M. Troyer, Solving strongly correlated electron models on a quantum computer, Physical Review A - Atomic, Molecular, and Optical Physics **92**, 1 (2015).

[31] P. Lunts, A. Georges, E. M. Stoudenmire, and M. Fishman, The hubbard model on the bethe lattice via variational uniform tree states: metal-insulator transition and a fermi liquid, Physical Review Research **3**, 023054 (2021), arXiv: 2010.06543.

[32] G. Kotliar and D. Vollhardt, Strongly correlated materials: Insights from dynamical mean-field theory, Physics Today **57**, 53 (2004).

[33] M. Potthoff, Two-site dynamical mean-field theory, Physical Review B **64**, 165114 (2001).

[34] J. M. Kreula, L. García-Álvarez, L. Lamata, S. R. Clark, E. Solano, and D. Jaksch, Few-qubit quantum-classical simulation of strongly correlated lattice fermions, EPJ Quantum Technology **3**, 1 (2016).

[35] H. N. Sá Earp and J. K. Pachos, A constructive algorithm for the Cartan decomposition of $SU(2^N)$, Journal of Mathematical Physics **46**, 082108 (2005).

[36] J. S. Pedernales, R. Di Candia, I. L. Egusquiza, J. Casanova, and E. Solano, Efficient quantum algorithm for computing n-time correlation functions, Phys. Rev. Lett. **113**, 020505 (2014).

[37] T. Steckmann and E. Kökcü, (2021), `Cartan Quantum Synthesizer`: https://github.com/kemperlab/cartan-quantum-synthesizer.

[38] M. S. ANIS *et al.*, Qiskit: An open-source framework for quantum computing (2021).

[39] B. Zhang, S. Majumder, P. H. Leung, S. Crain, Y. Wang, C. Fang, D. M. Debroy, J. Kim, and K. R. Brown, Hidden Inverses: Coherent Error Cancellation at the Circuit Level, arXiv:2104.01119 [quant-ph] (2021), arXiv: 2104.01119.

[40] A. Asfaw, A. Corcoles, L. Bello, Y. Ben-Haim, M. Bozzo-Rey, S. Bravyi, N. Bronn, L. Capelluto, A. C. Vazquez, J. Ceroni, R. Chen, A. Frisch, J. Gambetta, S. Garion, L. Gil, S. D. L. P. Gonzalez, F. Harkins, T. Imamichi, H. Kang, A. h. Karamlou, R. Loredo, D. McKay, A. Mezzacapo, Z. Minev, R. Movassagh, G. Nannicini, P. Nation, A. Phan, M. Pistoia, A. Rattew, J. Schaefer, J. Shabani, J. Smolin, J. Stenger, K. Temme, M. Tod, S. Wood, and J. Wootton., Learn quantum computation using qiskit (2020).

[41] B. Shaparenko and J. M. Cimbala, A simple equation for predicting aliasing frequency, (in press) International Journal of Mechanical Engineering Education (2012).

[42] E. Lange, Renormalized vs unrenormalized perturbation-theoretical approaches to the mott transition, Modern Physics Letters B **12**, 915–919 (1998), arXiv: cond-mat/9810208.

[43] M. A. Nielsen, The fermionic canonical commutation relations and the Jordan-Wigner transform (2005), unpublished.